## PAPER

Check for updates

# Bandgap recovery of monolayer MoS$_2$ using defect engineering and chemical doping†

Frederick Aryeetey, [ID] *[a] Sajedeh Pourianejad, [ID] [b] Olubukola Ayanbajo, [ID] [a] Kyle Nowlin,[b] Tetyana Ignatova [ID] *[b] and Shyam Aravamudhan [ID] *[a]

Two-dimensional transition metal dichalcogenide materials have created avenues for exciting physics with unique electronic and photonic applications. Among these materials, molybdenum disulfide is the most known due to extensive research in understanding its electronic and optical properties. In this paper, we report on the successful growth and modification of monolayer MoS$_2$ (1L MoS$_2$) by controlling carrier concentration and manipulating bandgap in order to improve the efficiency of light emission. Atomic size MoS$_2$ vacancies were created using a Helium Ion Microscope, then the defect sites were doped with 2,3,5,6-tetrafluro7,7,8,8-tetracyanoquinodimethane (F4TCNQ). The carrier concentration in intrinsic (as-grown) and engineered 1L MoS$_2$ was calculated using Mass Action model. The results are in a good agreement with Raman and photoluminescence spectroscopy as well as Kelvin probe force microscopy characterizations.

## 1 Introduction

Recent advances in materials research have focused on novel, atomically thin semiconducting materials. Starting with gapless graphene,[1] a broad family of two-dimensional (2D) dichalcogenide materials have been fabricated in monolayer and few-layers form.[2–4] These materials possess unique properties enabling creation of a new generation of flexible and ultrathin optoelectronic devices. Among this family, direct bandgap semiconducting monolayer molybdenum disulfide (1L MoS$_2$) is the most popular one.[5,6] There are numerous reports of successful Chemical Vapor Deposition (CVD) synthesis processes. Unfortunately, CVD grown 2D MoS$_2$ always contains sulfur vacancies resulting in the creation of unsaturated chemical bonds at the molybdenum atoms. Sulfur vacancies represented by dangling bonds may serve as active sites for chemical adsorption of species. They will also result in quenching and broadening of MoS$_2$ photoluminescence (PL) by bringing additional defective states that are not available in the perfect system.[7–12] These vacancies influence drastically the carrier concentration and exciton generation in a sample. In a perfect system two exciton states are formed at the $K$ and $K'$ point of MoS$_2$ Brillouin zone – exciton A (around 1.8 eV) and

exciton B (around 2 eV). In the presence of sulfur vacancies, interaction of exciton and free carrier gives rise to the formation of a many-body bound state, a negatively charged exciton, also referred as a trion. It is already known that the PL of monolayer MoS$_2$ can be enhanced by reducing concentration of the excessive electrons and related shift of oscillator strength between trions and excitons.[13,14] Various techniques have been employed to modulate optical properties of 1L MoS$_2$ by controlling free carrier density, namely electrical gating, gas physisorption,[13,15] and chemical doping.[16–19]

In this study, we first investigated intrinsic doping of as-grown monolayer MoS$_2$. We later modified monolayer MoS$_2$ using focused helium ion irradiation, consequently introducing monosulfur and disulfur vacancies predominately. The carrier concentration in as-grown and defected samples was linked with 2D MoS$_2$ optical response. Finally, we restored/enhanced PL of defected monolayer MoS$_2$ *via* chemical p-type doping.

## 2 Experimental procedures

### 2.1 Sample preparation

High quality 2D MoS$_2$ samples were grown at 650 °C on Si/SiO$_2$ substrates using a home-built CVD setup with a one-inch quartz tube fitted in Lindberg furnace equipment. Fig. 1a–d shows that the morphology and shape of 2D MoS$_2$ varies depending on the stoichiometric ratio of Molybdenum to sulfur : hexagon shape flakes grow when the ratio is 1 : 1, an uneven ratio will give rise to triangles. The SEM and Raman analysis confirm that the majority of MoS$_2$ flakes are monolayers, however, some flakes, especially hexagons, have small islands of second- and third-layer.

*[a]Department of Nanoengineering, North Carolina A&T State University, 2907 East Gate City Blvd, Greensboro, NC, 27401, USA. E-mail: saravamu@ncat.edu; Fax: +1-336-500-0115; Tel: +1-336-285-2810*

*[b]Department of Nanoscience, University of North Carolina at Greensboro, 2907 East Gate City Blvd, Greensboro, North Carolina, 27401, USA. E-mail: t_ignato@uncg.edu; Fax: +1-336-500-0115; Tel: +1-336-285-2820*

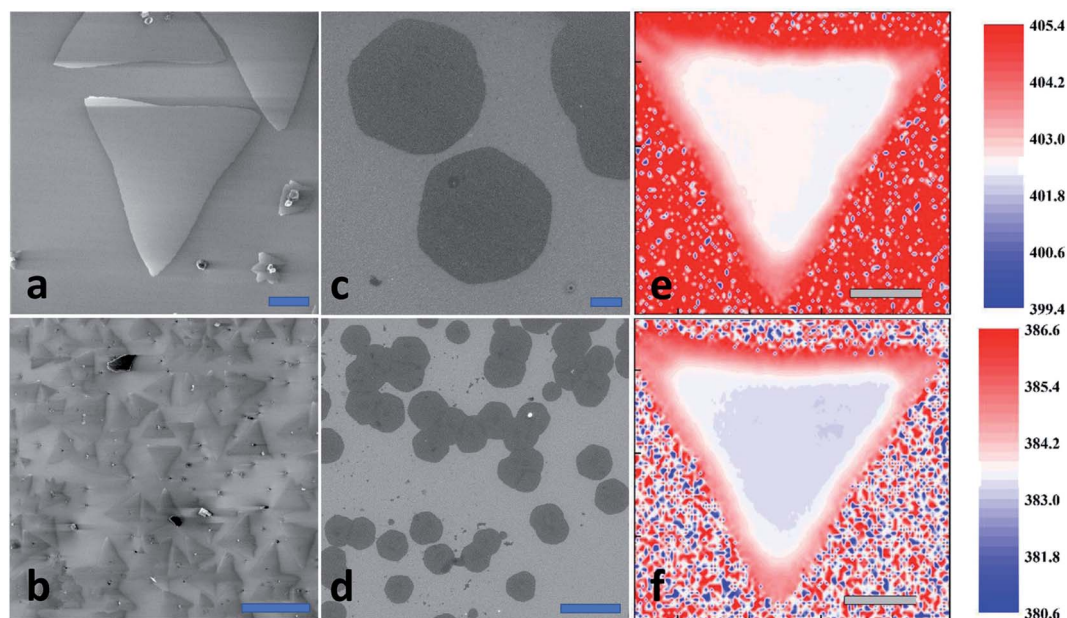† Electronic supplementary information (ESI) available. See DOI: 10.1039/d1ra02888j

Fig. 1  (a and b) Helium Ion Microscopy of as-grown $MoS_2$; (c and d) SEM images of $MoS_2$ transferred to conductive substrate for CAFM characterization; Raman map of $1LMoS_2$: (f) $E_{2g}$ at 383 cm$^{-1}$, and (e) $A_{1g}$ at 402 cm$^{-1}$. The scale bars in (a, d, e and f) are 5 μm, in (b) 50 μm, in (c) 500 nm.

$MoS_2$ samples were irradiated in a Zeiss Helium Ion Microscope operating at accelerating voltage of 30 kV with doses of (1) $1 \times 10^{13}$, (2) $5 \times 10^{14}$, (3) $9 \times 10^{14}$, (4) $1 \times 10^{15}$, (5) $5 \times 10^{15}$, (6) $9 \times 10^{15}$, and (7) $1 \times 10^{16}$ He$^+$ ions per cm$^2$. The exposure was performed using patterning software to raster the focused helium ion beam over a large area (up to 50 μm). A beam current of 5 pA was used for all exposures with dosage being controlled by exposure time. This resulted in the introduction of defects with inter-defect distances varying from 10.3 nm to 3.7 nm as we reported elsewhere.[20] Prior to doping, $MoS_2$ samples were placed in the middle of a CVD tube furnace and annealed at 250 °C for 1 hour. The samples were then soaked in a solution of 0.3 μmol ml$^{-1}$ of 2,3,5,6-tetrafluro7,7,8,8-tetracyanoquinodimethane (F4TCNQ) in Chloroform for 12 hours, then rinsed to remove unbounded F4TCNQ as suggested in.[21] Thereafter, the samples were heated on a hot plate at 100 °C for 30 minutes.

## 2.2  Characterization techniques

Photoluminescence (PL) and Raman spectra were recorded with a Horiba XploRa Confocal Raman Microscope at 532 nm of excitation. The laser power was kept below 0.5 mW to avoid thermal damage due to heating. Scanning Probe Microscopy was performed on an Oxford Asylum Research Atomic Force Microscope (AFM) MFP-3D Infinity.

Surface potential imaging was performed in amplitude-modulated mode with conductive Si tips coated with Pt/Ir (EFM-20, NanoWorld). The Asylum's ORCA™ module was used for conductive mode (CAFM). For this characterization, we transfered $MoS_2$ samples to a Si substrate coated with a 50 nm gold film using the wet KOH transfer method.[22] The I–V curves were recorded before and after modification of the $MoS_2$

samples, with the CAFM tip (CDT-NCHR-SPL) being engaged very gently with only a few nN of force being applied until the current signal stabilized. All above measurements were performed at ambient conditions. The X-ray Photoelectron Spectroscopy (XPS) data were obtained on a Thermo Fisher ESCALAB 250 Xi. The atomically resolved images of the $MoS_2$ sample were recorded using the Scanning Transmission Electron Microscope Nion Ultra HAADF-STEM 100 at Oak Ridge National Laboratory.

## 3  Results and discussions

By adjusting proper synthesis conditions, we grew 2D $MoS_2$ flakes with the area up to 270 μm$^2$ as shown on Fig. 1a–d. Scanning Electron and Helium Ion Microscopy allow for visualization of shape, lateral dimensions, and homogeneity of
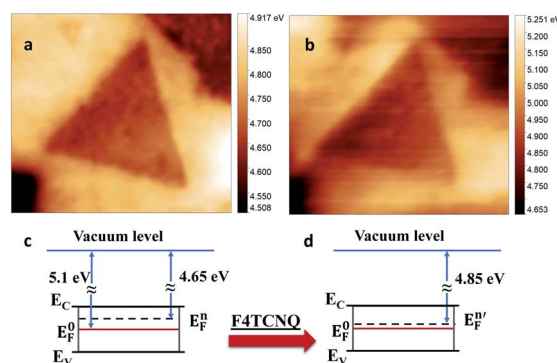


Fig. 2  The $MoS_2$ work function map acquired (a) before and (b) after p-doping with F4TCNQ; simplified sketch of $MoS_2$ electronic structure before doping (c) and after doping (d).

grown $MoS_2$ samples. However, these techniques do not provide quantitative information for the number of $MoS_2$ layers in a single flake. Confocal Raman spectroscopy is the most popular tool for reliable identification the $MoS_2$ layer number, as well as for doping and strain. The two prominent Raman peaks located around $402\ cm^{-1}$ and $383\ cm^{-1}$ assigned to the out-of-plane ($A_{1g}$) and in-plane ($E_{2g}$) phonon vibration modes respectively. The band separation $\Delta f = 19 - 20\ cm^{-1}$ corresponds to 1L $MoS_2$. With the increasing number of layers, the difference $\Delta f$ will also increase, for instance, $\Delta f = 21 - 22\ cm^{-1}$ corresponds to bilayer of $MoS_2$.

Our typical results of Raman mapping show spatial homogeneity of $E_{2g}$ (Fig. 1f) and $A_{1g}$ (Fig. 1e) over the $MoS_2$ flake area: the intensity and variation for both peaks were negligible, so we have identified as grown flakes as pristine monolayers. The pristine 1L $MoS_2$ exhibits a strong PL peak centered at 1.83 eV. However, the efficiency and broadening of $MoS_2$ emission is far from the theoretical limits of the direct band gap semiconductor material. It is already known that p-doping can

positively influence the optical properties of 1L $MoS_2$.[23–25] To prove this, we started with conducting ambient surface potential measurements using two-pass AM-KPFM on the as-grown sample. The work function value $\Phi_{sample}$ and, consequently, Fermi energy shift were calculated by equation:

$$\Phi_{sample} = e \times V_{CPD} - \Phi_{probe} \tag{1}$$

where $V_{CPD}$ is the charge potential difference between the sample ($MoS_2$) and the AFM probe, $e$ is elemental charge, and $\Phi_{probe}$ is the work function of the KPFM probe. The probe was calibrated with highly oriented pyrolytic graphite (HOPG) having a work function of 4.65 eV. The spatial distribution of $\Phi_{1LMoS2}$ for the as-grown sample is presented on Fig. 2a. It should be noted that for monolayer $MoS_2$ (no doping) the theoretical value of $\Phi_{1LMoS2}$ is equal to 5.1 eV[26] and Fermi energy is in the middle of bandgap. The measured value for as-grown 1L $MoS_2$ showed shift of Fermi energy towards conduction band by 450 meV (Fig. 2c) indicating intrinsic n-doping of as-grown sample. These results are in agreement with previous
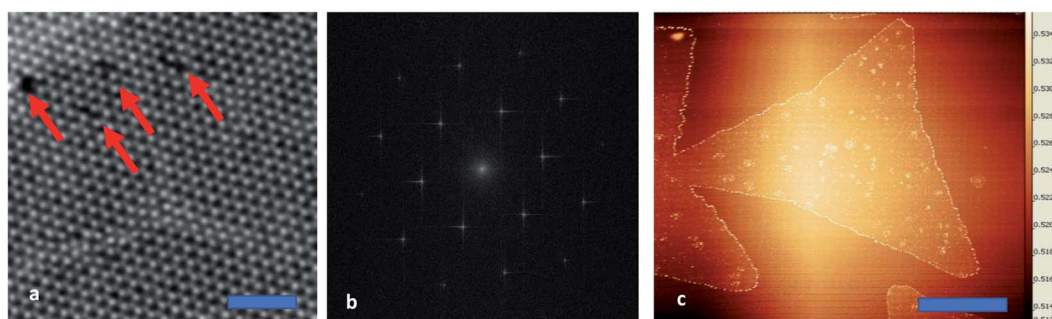


Fig. 3  The 1L $MoS_2$ irradiated at $1 \times 10^{14}$ He$^+$ ions per cm$^2$ dose. (a) HAADF–STEM image; scale bar is 4 nm; the red arrows indicate single and double sulfur terminations. (b) Fourier transform of STEM image. (c) AFM topography; scale bar is 4 μm.
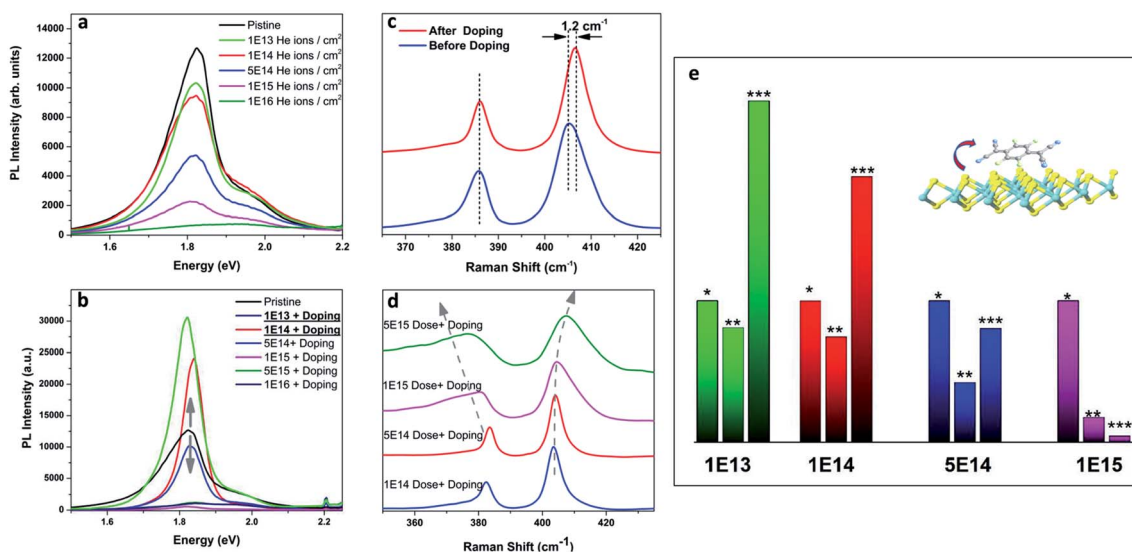


Fig. 4  (a) $MoS_2$ PL degradation with an increase of ion irradiation dose; and (c) Raman spectra before and after F4TCNQ doping (no ion irradiation) (b and d) PL and Raman spectra defected and doped $MoS_2$; (e) PL Intensity of pristine (*), defected (**), and defected and doped (***) $MoS_2$. Doses $1 \times 10^{13}$ and $1 \times 10^{14}$ provide perfect bandgap recovery and PL enhancement.

**Table 1** Calculations of carrier concentration for untreated and helium ion treated 1L $MoS_2$

| Applied doses (ions per $cm^2$) | Trion weight | Electr. conc. ($cm^{-2}$) |
|---|---|---|
| 0 | 0.38 | $1.56 \times 10^{13}$ |
| $1 \times 10^{13}$ | 0.383 | $1.53 \times 10^{13}$ |
| $1 \times 10^{14}$ | 0.390 | $1.62 \times 10^{13}$ |
| $5 \times 10^{14}$ | 0.410 | $1.72 \times 10^{13}$ |
| $1 \times 10^{15}$ | 0.460 | $2.2 \times 10^{13}$ |

reports on CVD grown 2D $MoS_2$ on Si/$SiO_2$, and are attributed mainly to the existence of natural defects such as sulfur vacancies.[27,28] As expected, a small increase in the local work function was found after incubation of as-grown sample with p-dopant F4TCNQ, such that the average Fermi energy shifted towards the center of bandgap by only 200 meV (Fig. 2b, c). According to DFT calculations,[29] the F4TCNQ molecule has a relatively weak adsorption on pristine $MoS_2$ surface. Therefore, we attribute this shift of Fermi energy to the interaction of F4TCNQ with the $MoS_2$ defect sites as further corroborated by TEM images in ESI (Fig. S5).† To have better control over optoelectronic properties of $MoS_2$, we propose here to combine doping and defect engineering. Our earlier work has demonstrated the ability to introduce defects by irradiating $MoS_2$ samples using Helium Ion Microscope,[20] although tuning of $MoS_2$ optical response had not been investigated earlier.

Multiple doses of Helium ion irradiation (from $1 \times 10^{13}$ to $1 \times 10^{16}$ $He^+$ ions per $cm^2$) were used to modify 1L $MoS_2$ electronic structure by generating sulfur vacancies. An AFM image of the irradiated sample is presented in Fig. 3c. The high-resolution HAADF-STEM image of the sample irradiated with the dose of $1 \times 10^{14}$ $He^+$ ions per $cm^2$ shows details of alternating symmetry of atoms arranged in hexagonal rings (Fig. 3a red arrows). Over this area, four defect sites are seen that would be available for adsorption and doping. There is also a $MoS_2$ grain boundary that is stitching together three parts of the 1L $MoS_2$ flake. Notably, there are no sulfur vacancies associated with broken symmetry near the grain boundaries.

Despite of the fact, that the Fourier Transform of the STEM image (Fig. 3b) confirms preserved of the Brillouin zones hexagonal geometry, PL intensity of this sample decreased by

30%, and for the next dose it dropped down further by 60% when compared to pristine 1L $MoS_2$ sample (Fig. 4a black-red-blue curves). To calculate the carrier concentration in the as-grown, defected, and defected-doped sample we applied the Mass Action model as introduced by J. Ross et al.[30] for a three level system.[14] According to this model, the relations between concentrations of excitons ($N_X$), trions ($N_{X^-}$) and the excess electrons ($n_e$) in transition metal dichalcogenides can be written as:

$$\frac{N_X n_e}{N_{X^-}} = \frac{4 m_X m_e}{\pi h^2 m_{X^-}} k_B T \exp\left(\frac{E_B}{k_B T}\right) \qquad (2)$$

where, $T$, $k_B$, $E_b$ are the temperature, the Boltzmann constant, and the trion binding energy (about 20 meV (ref. 31)) respectively. The effective mass of electrons is $m_e = 0.35\ m_0$ and the effective mass of holes is $m_h = 0.45\ m_0$. The $m_0$ is the free electron mass. The effective masses of an exciton and trion can be calculated as $m_X = m_e + m_h = 0.8\ m_0$, and $m_{X^-} = 2\ m_e + m_h = 1.15\ m_0$. Then, the trion PL intensity weight $\frac{I_{X^-}}{I_{total}}$ is related to the excess electron concentration $n_e$:

$$\frac{I_{X^-}}{I_{total}} = \frac{\beta n_e}{1 + \beta n_e} \qquad (3)$$

here $\beta$ is a constant, equal to $4 \times 10^{-14}$ $cm^2$. Using this model, we can calculate the electron concentration before and after doping:

$$n_e = \frac{1}{\beta}\left(\frac{I_{X^-}}{I_{total} - I_{X^-}}\right) \qquad (4)$$

We found that the trion PL weight in irradiated samples increases from 0.38 to 0.46 and correspondingly electron

**Table 2** Calculations of carrier concentration for defect-doped samples 1L $MoS_2$

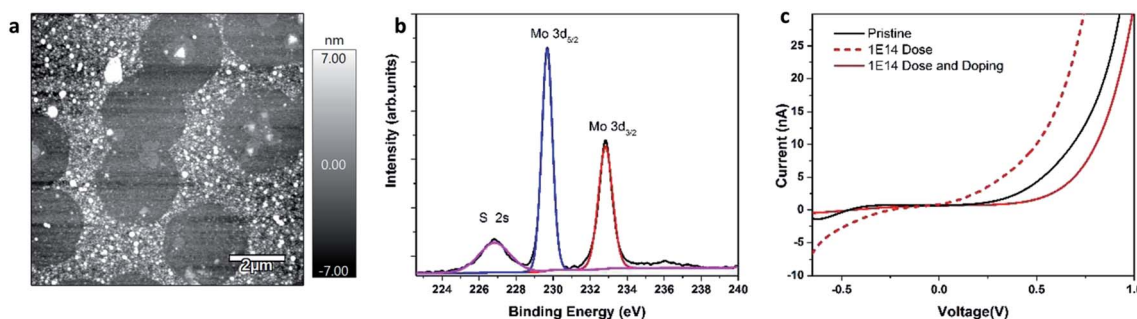| Applied doses (ions per $cm^2$) | Trion weight | Electr. conc. ($cm^{-2}$) |
|---|---|---|
| $1 \times 10^{13}$ | 0.370 | $1.40 \times 10^{13}$ |
| $1 \times 10^{14}$ | 0.306 | $1.13 \times 10^{13}$ |
| $5 \times 10^{14}$ | 0.310 | $1.12 \times 10^{13}$ |



**Fig. 5** (a) AFM topography of transferred $MoS_2$ on conductive substrate; (b) XPS core-level spectra of molybdenum 3d and sulfur 2 s; (c) I–V characterization for pristine and doped, defected and doped $MoS_2$.

concentration of doped 1L $MoS_2$ increases from $1.56 \times 10^{13}$ 1 $cm^{-2}$ to $2.2 \times 10^{12}$ 1 $cm^{-2}$ (Table 1). Indeed, $1 \times 10^{14}$ dose causes negligible damage. In contrast, $1 \times 10^{16}$ dose disrupts $MoS_2$ lattice symmetry completely.

A simple and effective chemical p-doping method was used to tune the carrier concentration in 1L $MoS_2$. The F4TCNQ molecule can easily bind to the sulfur vacancies and act as an acceptor. As we discussed above, Raman spectroscopy could be used to trace the doping effect in 1L $MoS_2$. In the case of p-doping, frequency of $E_{2g}$ peak should remain constant, but the frequency of $A_{1g}$ peak is blue-shifted.[32,33] Raman characterization of the F4TCNQ doped as-grown sample (untreated with ion beam) shows that the $A_{1g}$ peak position shifts by 1.2 $cm^{-1}$ while $E_{2g}$ peak position remains the same (Fig. 4c). However, after irradiation, $E_{2g}/A_{1g}$ modes are both red/blue shifted, and widened due to the appearance of new phonon modes. There is a shoulder (at 362 $cm^{-1}$) to the left of $E_{2g}$ mode, and one (at 415 $cm^{-1}$) to the right of $A_{1g}$ mode, which are assigned to a defect mode.[33–35] Both peaks are significantly enhanced after irradiation with helium ions.

After p-doping of defected samples, we observe a gigantic enhancement of $MoS_2$ PL for the dose of $1 \times 10^{13}$ and $1 \times 10^{14}$ (compare green and red curves in Fig. 4a and b), and PL recovery for the dose $5 \times 10^{14}$ (blue curves in Fig. 4a and b). There is no PL recovery for the doses $1 \times 10^{15}$ and higher. We attribute it to substantial damage in the $MoS_2$ lattice by the ion bombardment. The spectral shape of the PL peak is also changing with dosage. It slightly shifts towards visible range with increase of dosage (from 1.83 eV to 1.81 eV) due to decrease of the trion weight. It is slightly lower than reported for p-doped pristine 1L $MoS_2$ previously.[14]

We apply the Mass Action model to calculate carrier concentration after defect engineering and doping. Excess electron concentration decreased in comparison to the pristine sample from 1.56 to $1.13 \times 10^{13}$ $cm^{-2}$ (Table 2). Fig. 4e presents data for pristine, defect, and defect-doped samples. One can see that PL efficiency is increased for the $1 \times 10^{13}$ sample by 230% and for the $1 \times 10^{14}$ sample by 90%. We attribute it to a sufficient reduction of excess electron concentration and as a result, increase of exciton oscillator strength.

For $I–V$ characterization, 1L $MoS_2$ was transferred on the conductive substrate (Fig. 5a). The XPS characterization confirmed elemental composition Mo : S – 1 : 2 (Fig. 5b). The bias applied to the sample caused current flow into the conductive AFM tip, which was then recorded by a current amplifier. Fig. 4c shows the $I–V$ graphs of as-grown, irradiated, and irradiated-doped 1L $MoS_2$ measured by CAFM. The CAFM voltage was in the range of $-1$ V to 1 V. All samples: as-grown, doped, and defected and doped exhibited a clear non-linear slope of the $I–V$ curve, which is characteristic of a metal/ semiconductor junction. A clear difference is observed between the $I–V$ curves recorded on a pristine, irradiated, irradiated-doped samples. Particularly, in the forward bias regime, higher current response is measured at the same voltage ($-0.65$ V) for the irradiated compared to the as-grown and irradiated-doped $MoS_2$. After irradiation at ion dose of $1 \times 10^{14}$ and doping, defected-doped 1L $MoS_2$ showed a characteristic $I–V$ curve of an ideal Schottky diode compared to the as-grown sample and irradiated $MoS_2$ sample. The results of transport measurements are consistent with the Raman and Photoluminescence characterization confirming that the F4TCNQ molecules in solution can strongly withdraw electrons from $MoS_2$ layers.

# 4 Conclusions

In conclusion, we performed a systematic modification of the electronic structure of 1L $MoS_2$ by (a) gentle defect introduction using helium ion microscope with doses ranging from $1 \times 10^{13}$ to $1 \times 10^{16}$ ion per $cm^2$, and (b) subsequent p-doping of defected $MoS_2$ sites. Reduced PL intensity was restored and drastically enhanced due to the adsorption of p-type dopants (F4TCNQ molecules) by 1L $MoS_2$. We explain the $MoS_2$ bandgap recovery is due to decrease of excess electron concentration resulting in an increase of exciton oscillator strength. Our findings can be useful for improvement in the efficiency of light emission devices based on two-dimensional materials beyond $MoS_2$.

# Conflicts of interest

There are no conflicts to declare.

# Acknowledgements

# References

1 A. K. Geim and K. S. Novoselov, *Nat. Mater.*, 2007, **6**, 183–191.

2 W. Choi, N. Choudhary, G. H. Han, J. Park, D. Akinwande and Y. H. Lee, *Mater. Today*, 2017, **20**, 116–130.

3 S. Manzeli, D. Ovchinnikov, D. Pasquier, O. V. Yazyev and A. Kis, *Nat. Rev. Mater.*, 2017, **2**, 17033.

4 B. M. Bersch, S. M. Eichfeld, Y.-C. Lin, K. Zhang, G. R. Bhimanapati, A. F. Piasecki, M. Labella and J. A. Robinson, *2D Materials*, 2017, **4**, 025083.

5 K. F. Mak, C. Lee, J. Hone, J. Shan and T. F. Heinz, *Phys. Rev. Lett.*, 2010, **105**, 136805.

6 D. Jariwala, V. K. Sangwan, L. J. Lauhon, T. J. Marks and M. C. Hersam, *ACS Nano*, 2014, **8**, 1102–1120.

7 P. K. Chow, R. B. Jacobs-Gedrim, J. Gao, T.-M. Lu, B. Yu, H. Terrones and N. Koratkar, *ACS Nano*, 2015, **9**, 1520–1527.

8 J. Li, S. Hu, S. Wang, H. Kang, Z. Chen, S. Zhao, Y. Zhang, Y. Sui and G. Yu, *Mater. Lett.*, 2021, **290**, 129421.

9 M. Erementchouk, M. A. Khan and M. N. Leuenberger, *Phys. Rev. B*, 2015, **92**, 121401.

10 H. M. Oh, G. H. Han, H. Kim, J. J. Bae, M. S. Jeong and Y. H. Lee, *ACS Nano*, 2016, **10**, 5230–5236.

11 B. Chen, H. Sahin, A. Suslu, L. Ding, M. I. Bertoni, F. M. Peeters and S. Tongay, *ACS Nano*, 2015, **9**, 5326–5332.

12 T. Völzer, F. Fennel, T. Korn and S. Lochbrunner, *Phys. Rev. B*, 2021, **103**, 045423.

13 S. Tongay, J. Zhou, C. Ataca, J. Liu, J. S. Kang, T. S. Matthews, L. You, J. Li, J. C. Grossman and J. Wu, *Nano Lett.*, 2013, **13**, 2831–2836.

14 S. Mouri, Y. Miyauchi and K. Matsuda, *Nano Lett.*, 2013, **13**, 5944–5948.

15 T. Granzier-Nakajima, K. Fujisawa, V. Anil, M. Terrones and Y.-T. Yeh, *Nanomaterials*, 2019, **9**, 425.

16 D. Pierucci, H. Henck, Z. Ben Aziza, C. H. Naylor, A. Balan, J. E. Rault, M. G. Silly, Y. J. Dappe, F. Bertran, P. Le Fèvre, F. Sirotti, A. T. C. Johnson and A. Ouerghi, *ACS Nano*, 2017, **11**, 1755–1761.

17 A. Molle, F. Fabbri, D. Campi, A. Lamperti, E. Rotunno, E. Cinquanta, L. Lazzarini, D. Kaplan, V. Swaminathan, M. Bernasconi, M. Longo and G. Salviati, *Adv. Electron. Mater.*, 2016, **2**, 1600091.

18 Y. Cai, H. Zhou, G. Zhang and Y.-W. Zhang, *Chem. Mater.*, 2016, **28**, 8611–8621.

19 M. Yarali, Y. Zhong, S. N. Reed, J. Wang, K. A. Ulman, D. J. Charboneau, J. B. Curley, D. J. Hynek, J. V. Pondick, S. Yazdani, N. Hazari, S. Y. Quek, H. Wang and J. J. Cha, *Adv. Electron. Mater.*, 2021, **7**, 2000873.

20 F. Aryeetey, T. Ignatova and S. Aravamudhan, *RSC Adv.*, 2020, **10**, 22996–23001.

21 D. M. Sim, M. Kim, S. Yim, M.-J. Choi, J. Choi, S. Yoo and Y. S. Jung, *ACS Nano*, 2015, **9**, 12115–12123.

22 H. Van Ngoc, Y. Qian, S. K. Han and D. J. Kang, *Sci. Rep.*, 2016, **6**, 33096.

23 K. H. Kim, K. S. Kim, Y. J. Ji, I. Moon, K. Heo, D.-H. Kang, K. N. Kim, W. J. Yoo, J.-H. Park and G. Y. Yeom, *J. Mater. Chem. C*, 2020, **8**, 1846–1851.

24 K. Cho, M. Min, T.-Y. Kim, H. Jeong, J. Pak, J.-K. Kim, J. Jang, S. J. Yun, Y. H. Lee, W.-K. Hong and T. Lee, *ACS Nano*, 2015, **9**, 8044–8053.

25 J. Yang, H. Kawai, C. P. Y. Wong and K. E. J. Goh, *J. Mater. Chem. C*, 2019, **123**, 2933–2939.

26 L. Britnell, R. M. Ribeiro, A. Eckmann, R. Jalil, B. D. Belle, A. Mishchenko, Y.-J. Kim, R. V. Gorbachev, T. Georgiou, S. V. Morozov, A. N. Grigorenko, A. K. Geim, C. Casiraghi, A. H. C. Neto and K. S. Novoselov, *Science*, 2013, **340**, 1311–1314.

27 I. Sharma and B. R. Mehta, *J. Alloys Compd.*, 2017, **723**, 50–57.

28 W. H. Chae, J. D. Cain, E. D. Hanson, A. A. Murthy and V. P. Dravid, *Appl. Phys. Lett.*, 2017, **111**, 143106.

29 O. K. Le, V. Chihaia, V. Van On and D. N. Son, *RSC Adv.*, 2021, **11**, 8033–8041.

30 J. S. Ross, S. Wu, H. Yu, N. J. Ghimire, A. M. Jones, G. Aivazian, J. Yan, D. G. Mandrus, D. Xiao, W. Yao and X. Xu, *Nat. Commun.*, 2013, **4**, 1474.

31 K. F. Mak, K. He, C. Lee, G. H. Lee, J. Hone, T. F. Heinz and J. Shan, *Nat. Mater.*, 2013, **12**, 207–211.

32 B. Chakraborty, A. Bera, D. V. S. Muthu, S. Bhowmick, U. V. Waghmare and A. K. Sood, *Phys. Rev. B*, 2012, **85**, 161403.

33 H. Li, Q. Zhang, C. C. R. Yap, B. K. Tay, T. H. T. Edwin, A. Olivier and D. Baillargeat, *Adv. Funct. Mater.*, 2012, **22**, 1385–1390.

34 S. Mignuzzi, A. J. Pollard, N. Bonini, B. Brennan, I. S. Gilmore, M. A. Pimenta, D. Richards and D. Roy, *Phys. Rev. B*, 2015, **91**, 195411.

35 Y. Chen, S. Huang, X. Ji, K. Adepalli, K. Yin, X. Ling, X. Wang, J. Xue, M. Dresselhaus, J. Kong and B. Yildiz, *ACS Nano*, 2018, **12**, 2569–2579.